CCUS: 4014060

Advancing Carbon Storage in Offshore Louisiana: Evaluation and Modeling Potential of Two Major Depleted Reservoirs in Vermilion_014 Field

Ahmed Eleslambouly*, Mursal Zeynalli, Andreas Moncada, Ahmed Fathy, Seda Rouxel, Khalifa University of Science and Technology.

Abstract

In the Gulf of Mexico (GOM), current carbon capture and storage (CCS) projects have focused on the onshore parts of the GOM. However, there is growing interest in CCS in offshore GOM. At CCUS'22, the Bureau of Ocean Energy Management (BOEM) identified three depleted gas fields in the Vermilion protraction area as "Tier 1 Depleted Reservoirs" for potential CO_2 storage. Publicly available data indicates that the VR014 field has a very high capacity and seal efficiency per depleted sand reservoir. The present study assessed the potential for CO_2 storage in the two largest Vermillion 014 (VR014) depleted reservoirs: BIG2_1C (8200 ft) and CRISI2 (9800 ft). Regional and local geoscience investigations were integrated to build a detailed 3D geological model, including the depleted reservoir, seals, and intermediate wet sands, to assess the primary structural trapping mechanism of the depleted reservoirs. Further refinement was obtained by geostatistical property modeling and incorporating seismic inversion results to generate a robust property distribution. The final integrated geological model was then used for dynamic simulation of various CO2 storage scenarios. Additionally, seismic attributes and geological analysis were undertaken to further understand the subsurface heterogeneity and refine the simulation results. The feasibility of storing in the two depleted reservoirs was evaluated through integrated subsurface interpretation and static and dynamic modeling. This research yields promising results for storing up to 155 MMT of CO_2 in the VR014 Field BIG2_1C and CRISI2 reservoirs. A substantial volume of CO_2 could be trapped in residually and structurally trapped volumes in selective regions. Solubility and mineral trapping are also taking place in lower volumes compared to the other two main trapping mechanisms with considerable amounts. Additionally, the sealing capacity of the faults and seal rocks in both reservoirs was analyzed, ensuring secure containment of the stored CO_2. The injectivity, high injection pressures, and the reservoir/seal rocks properties present challenges for CO_2 storage within Vermilion reservoirs through advanced geoscientific modeling techniques and emphasizing their potential for carbon storage; this research provides an offshore green solution for large Gulf Coast industrial emitters. The significance of this work extends to the broader

understanding of CCS, providing insights into modeling, structural carbon storage, and the potential for large-scale future CCS projects in the offshore GOM.

Introduction

In the United States, CCS projects have mainly focused on onshore development. offshore CCS projects have been viable options overseas, and therefore, there has been recent interest in assessing the CO_2 storage potential of the offshore GOM (Wendt et al., 2022; Agartan et al., 2018). A recent study by the Bureau of Ocean Energy Management (BOEM) assessed and classified the potential of multiple depleted fields in the offshore GOM (Alonso et al., 2022). Depleted gas fields offer significant advantages for CO_2 storage, leveraging extensive documentation from the exploration and production phase, medium to large-scale storage capacity, proven trapping integrity, and minimal pressure perturbations. Additionally, utilizing and modifying existing equipment enables cost savings and expedites projects (Hannis et al., 2017). However, the BOEM analysis was a regional scoping study requiring more field-level investigations. The specific potential of selected fields for actual CCS development requires higher-resolution study. Among the identified "Tier 1 Depleted Reservoirs" for potential CO_2 storage, three depleted gas fields, VR39, VR014, and VR076, in the Vermilion protraction area, could be of particular interest. In our study, we focus on the Vermillion 14 gas field (**Figure 1**).
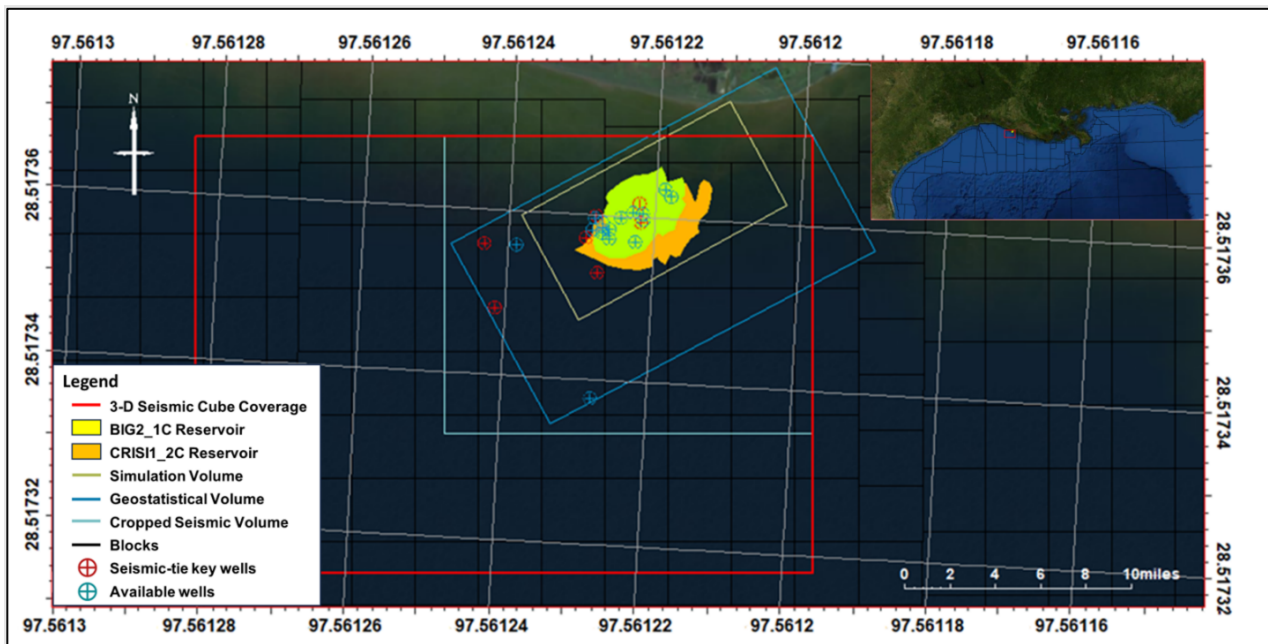

Figure 1 Satellite Imagery map of the study area, highlighting key components of the analysis work and dataset utilized during the study. The top right corner map shows the global view location of the zoomed-in map.

These fields have produced more than 1.3 trillion BOE since 1953, showing considerable volume potential for CO_2 storage with only one producer left in the three fields. A comprehensive review of the publicly available data covering 779 formerly producing reservoir intervals in the Vermilion block indicates that the VR014 field has the highest potential capacity and seal efficiency per depleted sand reservoir (**Figure 2**).
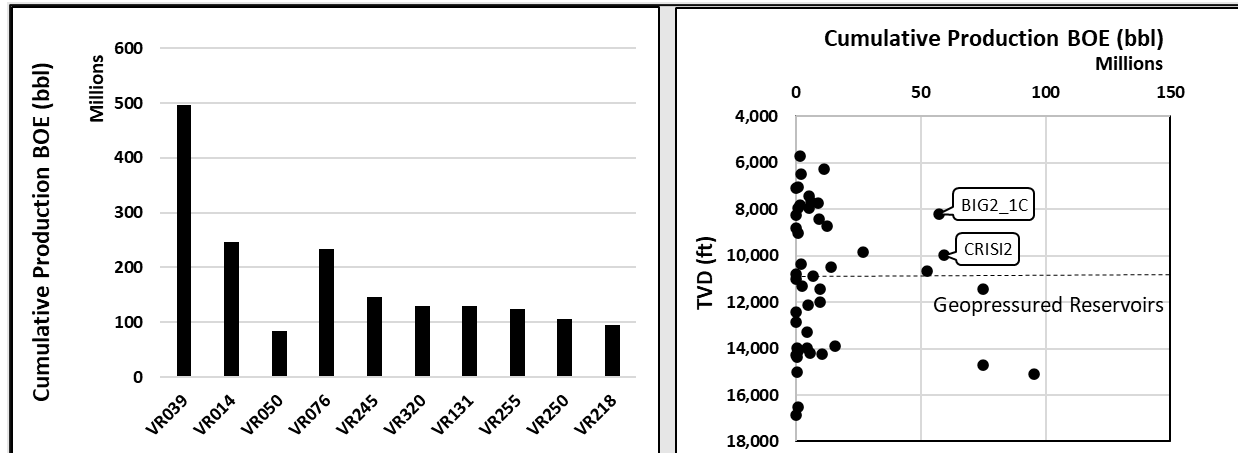
Figure 2 Cumulative production BOE history per field (left), and reservoir for Vermillion014 field (right), highlighting the two main targeted reservoirs for CO_2 storage.

Herein, we investigated at field-scale the suitability of the VR014 field for offshore CCS development by focusing on the potential for CO_2 storage and addressing the conditions and challenges associated with CO_2 sequestration in the two largest depleted reservoirs within VR014: BIG2_1C (7900 ft) and CRISI2 (9800 ft). In addition, both reservoirs are located between two major listric faults and form four-way closure traps therefore not relying on fault closure, eliminating one sealing risk factor. The feasibility of storing substantial amounts of CO_2 was evaluated through integrated subsurface interpretation combined with static and dynamic modeling to understand reservoir storage capacity, seal efficiency, CO_2 plume behavior, and trapping mechanisms. For this, a detailed 3D geological model, including the two reservoirs and related sealing units, was built using public wells data and a 3D seismic survey (**Figure 1**).

Materials and Methods

The present study integrates twenty-three wells obtained from the Bureau of Ocean Energy Management (BOEM) with available petrophysics dataset and additional reports from previous hydrocarbon production processes. In addition, a 3-D PSTM seismic cube retrieved from United States Geological Survey (USGS) archives, covering an area of 525 mi^2, including most of the Vermillion shallow waters offshore area (**Figure 1**). These datasets are integrated to build a heterogeneous geostatistical model of the two vertically stacked reservoirs aimed for CO_2 storage.

Petrophysical Characterization

A conventional petrophysical analysis approach was used to identify and compute the reservoir/seal properties such as total and effective porosities ($\Phi t, \Phi e$), shale volume (Vsh), initial water saturation (S_w), and net to gross (NG) (**Table 1**). The Vsh was determined using Larionov's equation (Larionov 1969). The $\Phi t, \Phi e$ values for the interval of interest were calculated using a different logs combination based on available well data. The determination of water resistivity (Rw) and cementation factor (m) for the Mount Messenger Formation used Pickett's plot method (Pickett 1972). This approach involved plotting effective porosity against deep resistivity (Rt) values. Water saturation (Sw) was assessed using the Indonesian equation. Four main lithologies were observed from the sidewall core descriptions, including clean and silty sands, silt, and shales. The sand grains are fine-grained and well-sorted, with varying shale content between clean and silty sands in the reservoir sequence. Reservoir core descriptions show that both reservoirs are characterized by fine-grained, silty sandstones. These facies were used to manually interpret the electrofacies and calibrate them based on core data availability. The narrow spacing of the wells allows high confidence in facies interpretation to create reservoir rock types (RRT). The side well core tests show

permeability trends against porosity for each facie. A nonlinear regression model was used to derive the poro-perm relationship for each facies (**Figure 3**). These relationships were used to compute continuous permeability log estimates based on each interpreted RRT. After identification of the reservoir pay and upper and lower seal, well correlations were carried out to attest the thinning or thickening of the reservoir and to constrain the seismic surface later on during modeling stage.
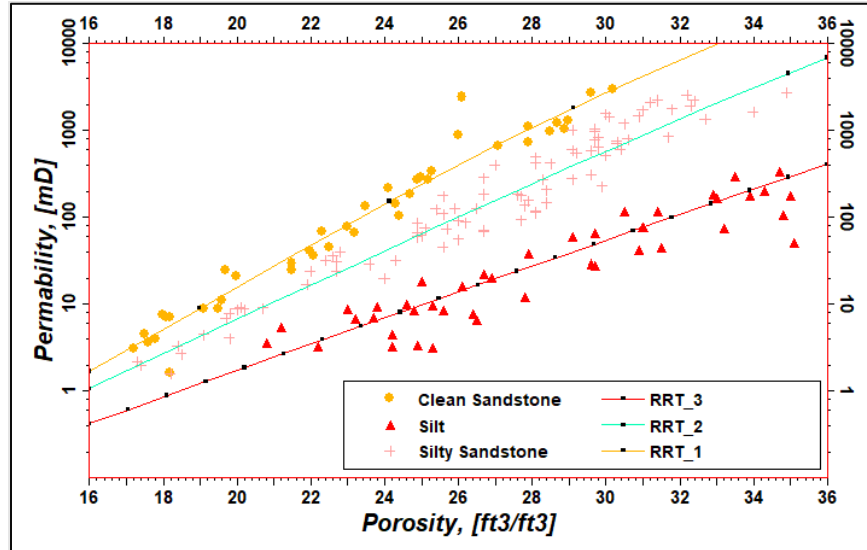

Figure 3 Porosity against permeability cross-plot with three RRT classifications

The formation water salinities were calculated from the formation water (*Rw*) resistivity at reservoir temperatures and cross-checked with SP logs at mud properties, as discussed by Ushie (2001). The reservoir temperatures were computed using the bottom hole temperature gradient. The final estimated reservoir properties are summarized in (**Table 1**).

Table 1 Summarized and average reservoir properties of the two depleted reservoirs

Reservoir Unit	Depth TVDSS (ft)	Φ (%)	Perm. (mD)	Initial Sw (%)	Temp (F)	Lithology	FW Salinity (ppm)	Gross (ft)	N/G	Area (Acres)
BIG2_1C	8209	29	316	28	186	Fine-grained silty sands	8721	180	0.81	8756
CRISI2	9974	27	274	25	215	interbedded with silt	12457	140	0.86	10246

Seismic Interpretation, Attributes, and Inversion

Seismic-well ties were performed for six key wells with a complete dataset including density, sonic, and checkshot data. (**Figure 4**) to recognize the targeted horizons identified by the log interpretation and visually inspect the seismic facies and associated amplitude changes. Two main horizons were interpreted for each reservoir unit, including the reservoir horizon and the top of upper-seal units (**Figure 5**). The field's major faults were mapped where the vertical displacement of the reflectors was recognized. Meanwhile, outside the seismic coverage, fault geometry was extrapolated by propagating the visible deep fault segment to the shallower parts. The field is a four-way anticlinal closure trending NE-SW and terminated to the north by a major listric fault that propagates to the seafloor and a synthetic fault towards the central part of the field that mainly affects the CRISI2 reservoir interval at deeper depth with more throw.
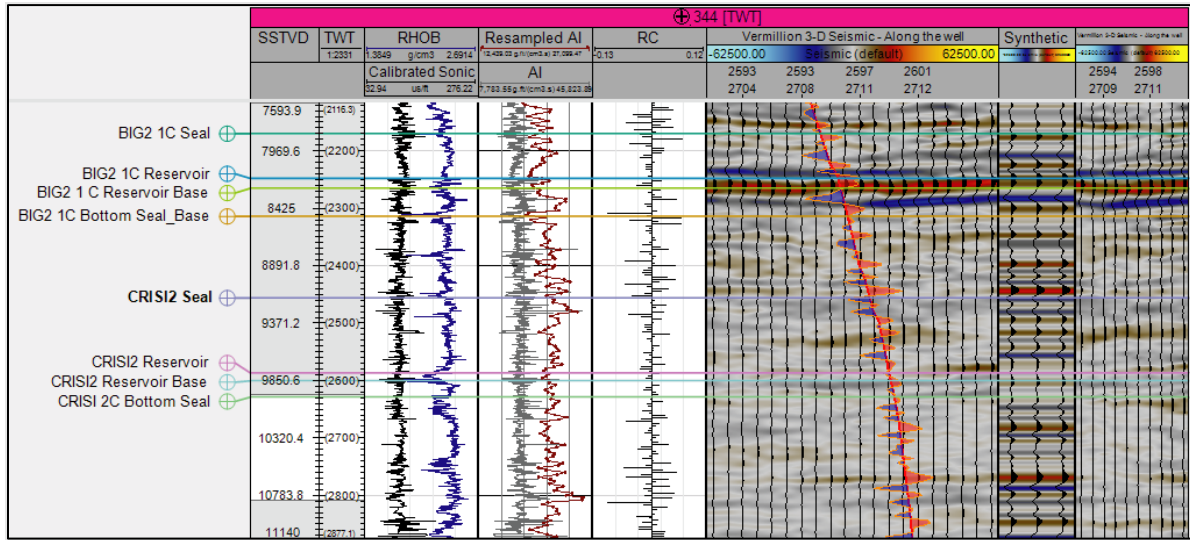
Figure 4 Synthetic seismogram of 344 well showing good match with real seismic data.
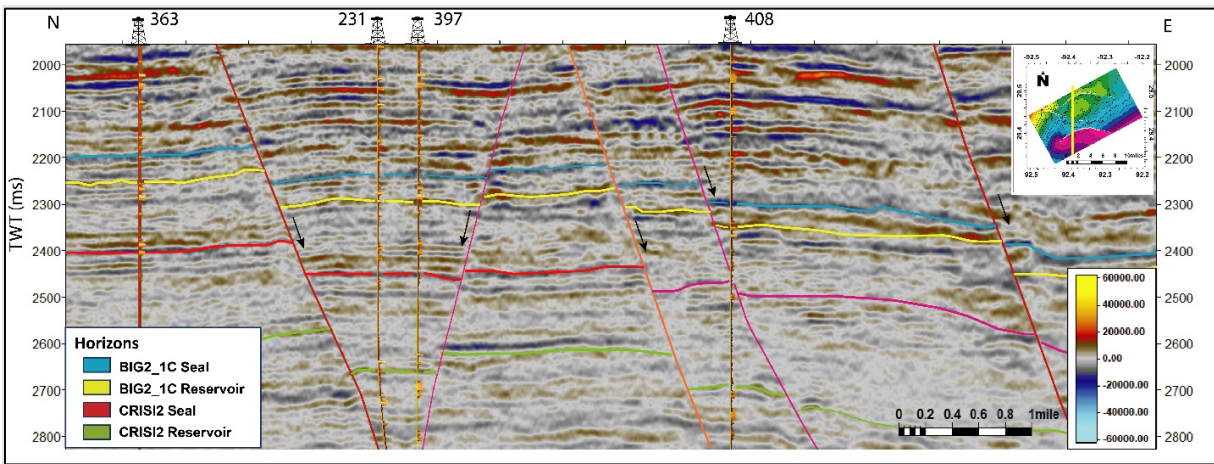

Figure 5 N-S interpreted seismic section showing the modeled horizons and faults.

Furthermore, several seismic attributes described in **Table 2** have been created (Petrel, OpenDtect) to investigate the subsurface heterogeneity, lithological changes, and bed geometry at both reservoir and seal levels. These quantitatively derived properties from the 3D seismic data were used to understand the rock facies, stratigraphic features, and fluid distribution in VR014, to reveal potential weakness in the seal or the heterogeneity in reservoir properties.

Table 2 List of seismic attributes aimed towards the field subsurface characterization.

Attribute	Description and Utilization
Acoustic Impedance	large contrasts indicate significant changes in lithology, e.g., tight (shaly/silty) sandstone transitioning to porous/clean sandstone or fluid content changes (water-filled to gas/hydrocarbon-filled sands).
RMS Amplitude	detects amplitude changes caused by stratigraphic features or fluid fills that are physically different and well bounded from their surroundings, thereby giving off high-density contrast signatures.
Coherency	derived from reflection discontinuity or large angle dips in reflections, this attribute is useful for delineating structural features.
Instantaneous frequency	detects lateral changes in lithology, increasing frequency indicates bed thinning or pinching out. As a rock property indicator, gas-filled sands have lower instantaneous frequency with respect to water-filled sand.

Energy Attenuation	measures the decrease in seismic energy as it travels through the subsurface, valuable aid in identifying areas with potential hydrocarbon accumulations or geological anomalies.
Envelope	represents the reflection strength due to impedance contrasts to show the effects of thin bed tuning, lateral changes in porosity, and other lithologic variations.
Spectral Decomposition	analyzes the frequency content of seismic data at various depth, useful for identifying reservoir compartments, faults, and stratigraphic variations by highlighting specific frequency components associated.

Each attribute listed in **Table 2** was generated within specific time windows centered on the target individual seal or reservoir horizon interpretations. Typical assessment window value ranges from 20ms to 50ms, while in some cases, the process considered time windows bounded by the nearest significant peak/trough events above and below the target interpretation. The extracted attribute properties are then superimposed on respective horizon gridded maps for geological interpretation and validity. Individual frequency slices were assessed and then selectively combined into RGB display.

The Post-stack seismic inversion technique is often used to estimate parameters using appropriate models from seismic (Veeken and Da Silva 2004). Post-stack seismic inversion is a critical tool for subsurface characterization, addressing heterogeneity, facies variations, and property transformations across a field while facilitating risk assessment. We used a model-based acoustic impedance (AI) inversion (Hampson-Russell software) by transforming seismic data into pseudo-AI impedance logs at every trace. Model-based inversion uses an iterative forward modeling and comparison procedure. A priori model is iteratively updated based on minimizing the error, hereby least-square error, between real seismic data and a synthetic dataset generated from the a priori model until the error reaches an acceptably low threshold value (Russell 1988).Seismic inversion requires a seismic-to-well relationship; thus, we used the six key wells previously defined. The inversion was applied to a cropped volume matching the field and the structural model geometry (**Figure 1**). A simple initial AI model was constructed by Kriging interpolation of well-log data to approximate a 3D low-frequency impedance model. This low-frequency model is essential for relative to absolute property value conversion. As a solution, a model with a very minor variation is adopted. One benefit of model-based inversion is that it produces acceptable results even with irregular wells distribution and average seismic quality, as in the VR014 case. Inversion results were validated by a series of blind wells tests. To derive a singular reservoir property from AI such as porosity and *Vsh*, a Neural Network (NN) were trained validated, and tested. Following this, property time slices are constructed at seismic horizons, employing the arithmetic mean function at time intervals representative of the reservoir's average thickness.

Structural Model

The subsurface model went through various stages and integration of the results to create a geo-cellular model matching the subsurface reservoir conditions. The seismic horizons were used to produce two-way time (TWT) surfaces. Both generated surfaces and interpreted faults were converted from time to depth domain (**Figure 6**) using a velocity model derived from all legacy checkshots from the field and served as the basis for building the static reservoir model.
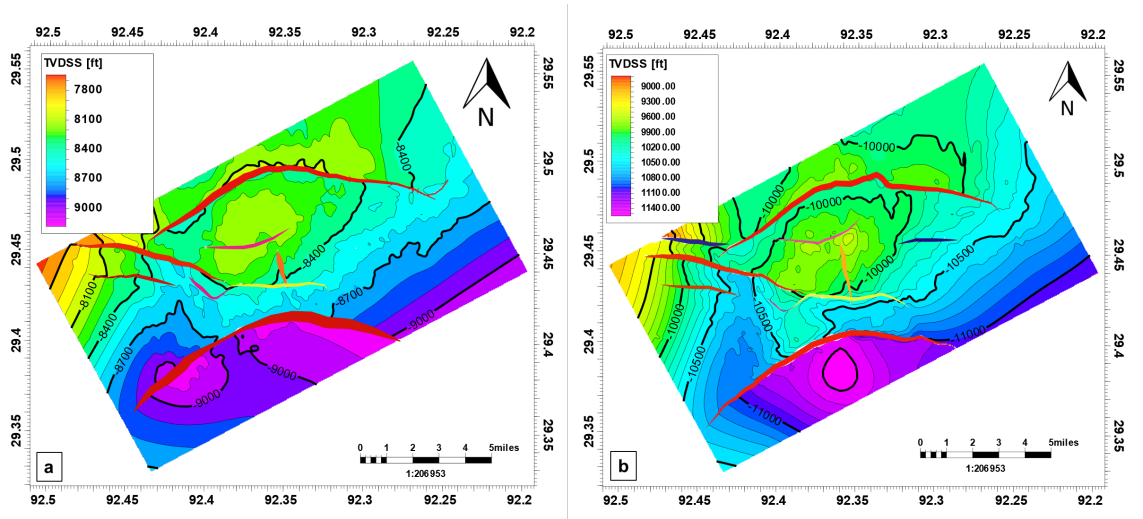
Figure 6 TVDSS depth contour maps a) BIG2_1C top surface, b) CRISI2 top surface

The formation tops identified from wells were integrated with the depth surfaces to construct a surface for each layer. The 3D structural model was constructed using the pillar gridding process. In the second step, the surfaces were imported into the model, taking into account the available observational data to create a stratigraphic subdivision. The model is constructed based on seven zonations, including the upper & lower seals, depleted sands for each reservoir unit, in addition to one transitional zone between the two reservoirs consisting of wet sands and shaly sequences (**Figure 7**). The layering was chosen to fit with the target simulation requirements. The vertical resolution of the modeled zonation varies from a high of 8 ft at the two reservoir zones to 20-40 ft at other intervals. This resulted in an intricately layered model, characterized by small XY cell dimensions (200×100 ft), to serve as a valuable tool to estimate the CO_2 storage capacity and for reservoir management and the prediction of plume behavior.
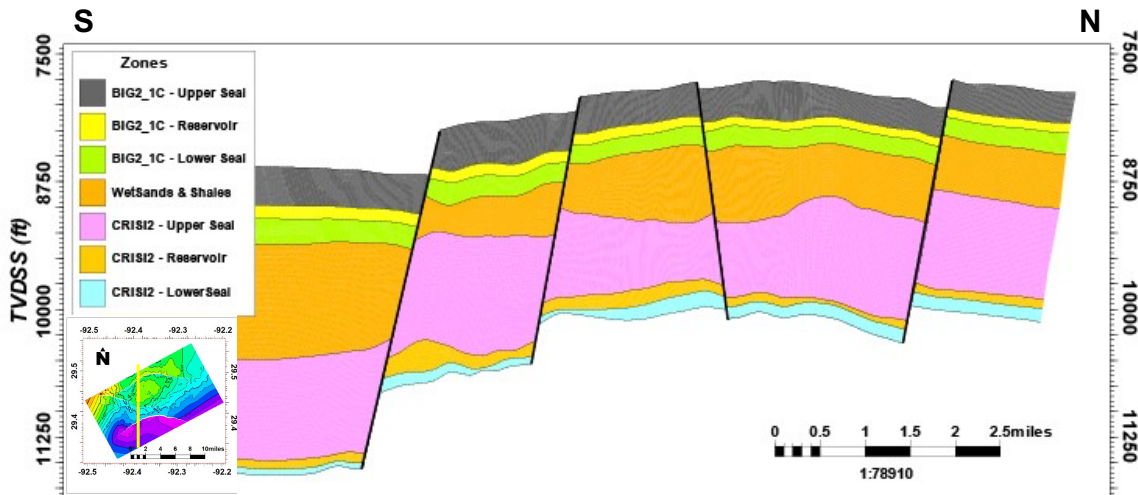
Figure 7 A N-S cross-section with main zonations overlay obtained from the 3D structural framework, aligned parallel to the seismic section line and perpendicular to the existing geological structures.

Reservoir Static Model

The objective of static property modeling was to construct a detailed heterogeneous model that incorporates the seven zonations mentioned earlier to establish a robust representation of both vertical and lateral

heterogeneity at various scales, encompassing individual wells, multiple wells, and the entire field in depleted conditions. The two reservoirs of interest were modeled at the depleted stage, and the current remaining hydrocarbon saturations within those reservoirs were calculated based on the recovery data. Upscaled values were computed by averaging the properties within each zone. For facies properties, the prevailing approach involved selecting the discrete value that was most prominently represented in the log. Meanwhile, the arithmetic average method was applied for other properties, including Φ_e, temperature, permeability, and S_w. The grid population was given a facies type based on the upscaled facies from wells. Given the lack of core information for shale lithologies, shale facies types were manually assigned by using a normal distribution, assuming a range between 0.01-0.003 mD as per the well report for very shaly sequences.

We applied a stochastic facies modeling approach to fill all cells in the model with lithofacies. This method is more suitable due to the lack of extensive data and of deep understanding of the depositional reservoir patterns and their architectures. The spatial distribution of the facies and other properties is based on a three directional geostatistical variogram: vertical, major, and minor for all layers. The major direction was defined towards the main deposition and sediment influx, revealed by seismic attributes and inversion trends. Data analysis was applied for all properties to assist the variograms and quality control the normal distribution associated with each facies type. The probability distributions shape the reservoir facies or property ranges and vertical trends across the reference upscaled cells. The distribution of ϕ and permeability of each zone is determined by a variogram per facies to increase the accuracy of populated cells and their estimations (**Figure 8**).

Within the reservoir zone, a horizontal trend is employed through seismic artificial intelligence, utilizing derived porosity and *Vsh* content slices. This approach, akin to co-kriging, is instrumental in aligning with the reservoir facies, porosity, and *Vsh* trends. Despite challenges posed by low seismic resolution, it is noteworthy that the cell value remains unaffected by co-kriging. Instead, it is governed by a constrained trend driven by seismic data, facilitating extrapolation/interpolation away from wells. In contrast, certain properties, such as temperatures and pressures, exhibit a greater reliance on true vertical depth (TVD), and were modeled as a depth-dependent function. The temperature model is constructed by applying the kriging function across all available well data. This methodological refinement ensures a more nuanced and accurate representation of subsurface conditions, enhancing the overall reliability of the study's findings. The outcomes of scaling up facies and rock properties have undergone rigorous validation to ensure the preservation of key heterogeneities influencing flow after the log scaling process by analyzing the corresponding histograms and the distribution shapes of input data, interpolated data, and well-log data should exhibit similarities or semi-similarities.

The original free gas-water contact (FWL) is determined using well logs and pressure data and compared to the seismic attribute's response for initial saturation height modeling in the two reservoirs. Saturation height modeling employs the Leverett et al., (1942) equation with iterations performed post-initial volume calculations to match produced volumes and water saturations with the current unproduced volume. Pressure depletion emerged as the predominant driving mechanism during primary recovery of hydrocarbons. Moreover, water drive was found to be a supportive secondary mechanism for production.

Furthermore, precise calculation of water saturation prior to injection is crucial, as it highly influences CO_2 solubility and residual trapping capacities (Mkemai and Gong, 2020). For example, in the solubility trapping mechanism, the trapping capacity is directly related to the contact of brine and CO_2 within the formation, especially for long-term storage duration. This quantifies the molality of the intra-aqueous species of bicarbonate in particular, which is closely related to water saturation, its distribution, and flow behavior at the depletion stage (Fathy, et al., 2023). Therefore, current water saturations were estimated and accounted for both BIG2_1C and CRISI2 reservoirs utilizing the recorded data of the field history, including recovery efficiency (*RE*), initial water saturation (S_{wi}), gas initially in place (*GIIP*), reservoir pore volume (V_p), and other parameters. The results of these calculations are listed in **Table 3**.

Table 3 Summary of the recorded data and computed depletion fluid saturations for BIG2_1C and CRISI2 reservoirs.

Parameter	BIG2_1C	CRISI2
Reservoir Pore Volume (V_p), bbl	$2768 * 10^6$	$3136 * 10^6$
Initial Water Saturation (S_{wi}), %	28	25
Gas Initially in Place ($GIIP$), MCF	$4919.60 * 10^{16}$	$5648.6 * 10^{16}$
Recovery Efficiency (RE), %	65	56
Remaining Gas Volume (V_{rg}), MCF	$1721.86 * 10^{16}$	$2485.38 * 10^{16}$
Remaining Gas Volume (V_{rg}), bbl	$697.536 * 10^6$	$1034.88 * 10^6$
Depletion Water Volume (V_{rw}), bbl	$2070.464 * 10^6$	$2101.12 * 10^6$
Depletion Water Saturation (S_{wd}), %	74.8	67

Finally, fault seal and transmissibility are essential for simulation and dynamic modeling to discern their effects on hydrocarbon entrapment and are even more critical when it comes to safe CO_2 storage. Shale Gouge Ratio (SGR) and smearing analysis, coupled with the static model, were undertaken for this purpose. The fault seal analysis workflow starts with the populated *Vsh* volume by calculating the smearing, thickness, and permeability of the faults against the *Vsh* volume. The resulting product is the fault transmissibility multiplier, which was used in the dynamic simulation to constrain the fault's properties. The calculation of fault transmissibility in this study was performed using equation (6) in (Manzocchi et al., 1999):

$$\log K_f = -4SGR - \frac{1}{4}\log(D)(1 - SGR)^5 \tag{6}$$

where, D represents the fault displacement in ft, and SGR is the ratio of shale gouge. The equation below incorporates permeability, dimensions of the grid cells, and the ratio of fault thickness to permeability. The computed values were used in the dynamic modeling to examine the faults relation to plume growth and migration across the faults. This formula is utilized to quantify the SGR based on the given fault displacement value. Equation (7) for calculating the shale gouge ratio (SGR) according to Yielding et al., (1997) is as follows:

$$SGR = \frac{\sum \left[Zone_{thickness} \times zone_{clay_{fraction}} \right]}{Fault_{throw}} \times 100\% \tag{7}$$
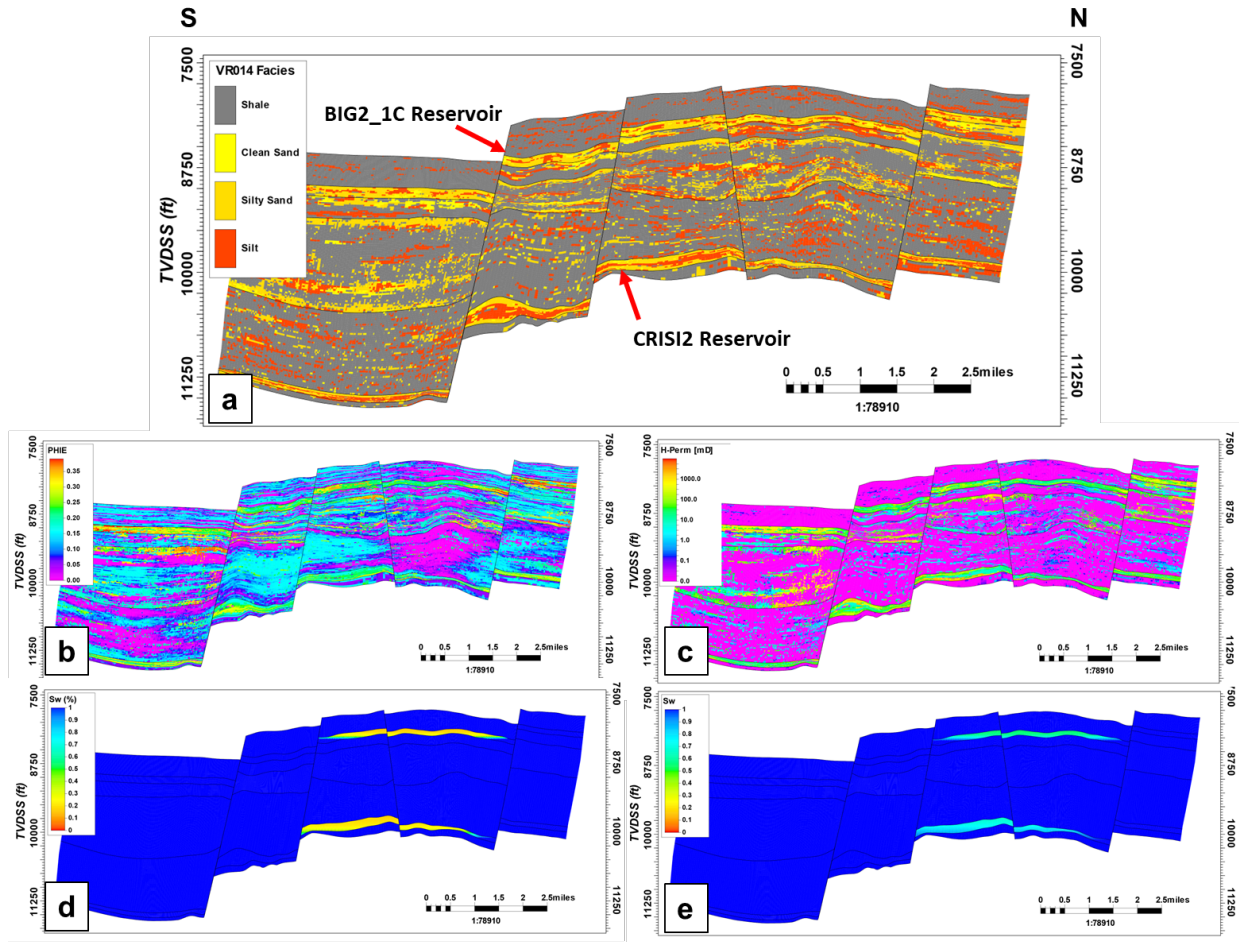
Figure 8 N-S Distributed property cross sections. a) facies, b) effective-porosity, c) horizontal permeability, d) initial water saturation, and e) depleted water saturation.

Reservoir Dynamic Modeling

The dynamic simulations of CO_2 storage in VR014 focused mainly on CO_2 plume migration, active trapping mechanisms, and supercritical CO_2-brine interactions in a clastic reservoir with shale, silt, and sandstone units. The performance of CO_2 injection and storage has been evaluated primarily in two reservoir units, including BIG2_1C and CRISI2. The simulation studies commenced by importing the static reservoir model with heterogeneous porosities, permeabilities, depleted water saturations, and other crucial properties to CMG. As it was previously mentioned, the pore pressures and temperatures were also embedded into the static model as a function of depth. It is noteworthy that, although depleted, the reservoir pressures, as well as temperatures, were sufficient to ensure the injection of supercritical-state CO_2 gas. Moreover, the size and intricacy of the static model resulted in a reliable portrayal of CO_2 plume migration and facilitated a comprehensive investigation of various trapping mechanisms.

Model Description

Dynamic reservoir modeling has been carried out using the CMG GEM compositional simulator. The input porosity field imported with the static model ranges from ultra-low values to over 35%, with an average porosity of 29% and 27% for the BIG2_1C and CRISI2 reservoirs, respectively (**Figure 8b**). Likewise, the model demonstrates significant variation in horizontal permeabilities, spanning from 0.003 mD in shaly

zones and seals to more than 1000 mD (**Figure 8c**). The average horizontal permeabilities for BIG2_1C and CRISI2 are 316 mD and 274 mD, respectively.

Moreover, the hydrocarbon composition was characterized using the wellsite analysis data released by BOEM. The data indicated that in the VR014 field, the hydrocarbon composition is ~95% methane and ~4% ethane, alongside various other compounds. History-matching of the primary recovery phase of hydrocarbons has been skipped, and the simulation was initiated at the reservoir depletion stage. The projected average water saturations before CO_2 injection stood at 75% for BIG2_1C and 67% for CRISI2 reservoirs (**Figure 8c**).

In addition, the pressures embedded in the model are depth-dependent and were calculated using the gradients obtained from the BOEM pressure surveys. The hydrostatic pressure gradient of 0.471 psi/ft was utilized for the overall model, excluding the two pressure depleted reservoir sections with the updated gradient of 0.167 psi/ft. A preliminary sensitivity analysis was also undertaken to ascertain the optimal number of CO_2 injection wells and devise a suitable injection strategy. As a result, the simulation model integrated three injectors for each reservoir.

Subsequently, gas injection persisted for 50 years, spanning from 2025 to 2075, followed by a subsequent 100-year post-injection storage period from 2075 to 2175 to study CO_2-brine interactions. The selection of the injection duration has been determined through a sensitivity analysis of the injected gas quantity. However, in actual field implementation, this factor should be exclusively guided by project economics and the accessibility of CO_2 for capture. The well locations for each reservoir were selected based on the reservoir geometry, petrophysical properties, and pre-injection saturations in the depleted reservoirs (**Figure 9**). Notably, the wells are strategically perforated in the thicker zones and the water leg, aiming to optimize CO_2 trapping as it migrates from the aquifer to the top of the reservoir, maximizing the contact area.
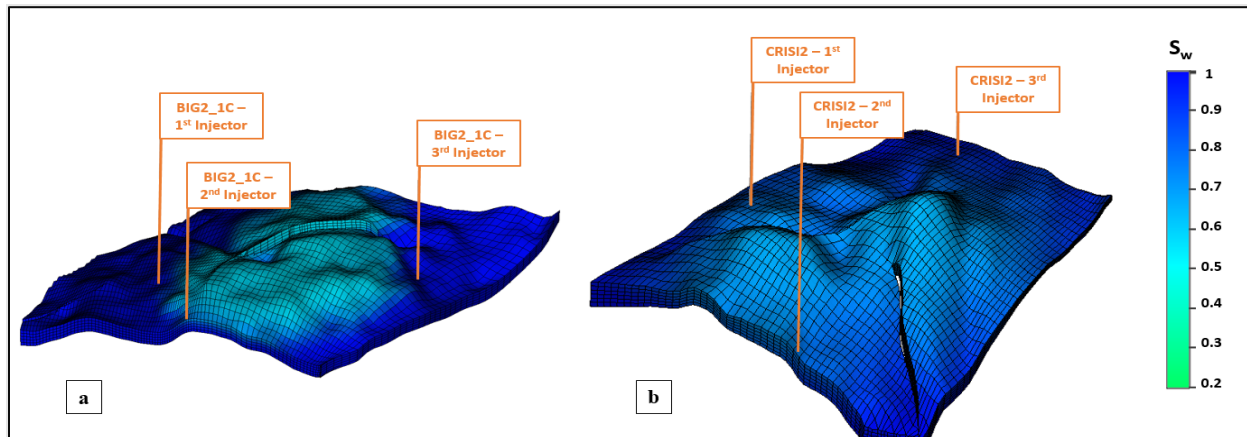

Figure 9 Pre-injection water saturation distribution in the cropped 3D maps illustrating well placement in a) BIG2_1C and b) CRISI2 reservoirs.

Furthermore, specific constraints were established for the injectors, encompassing the reservoir gas rate (BHG) and bottom hole pressure (BHP). The constraints on BHP for the upper and lower reservoirs were set at 4800 psi and 5790 psi, respectively. These values were determined based on safety considerations for CO_2 storage. In this context, the mud weights from **Figure 10** were considered as the fracture pressures, beyond which there is a risk of breaking the formation or faults reactivation, causing CO_2 leakage into shallow potable aquifers or the atmosphere through the fractured caprock, faults, and overburden. In general, fracture pressures are important early in the field's lifespan at the primary production stage to design the mud weights for the drilling of new wells (Zhang et al., 2023). Moreover, as the field proceeds to the depletion stage, it becomes crucial for CO_2 containment for long-term and secure storage (Fathy et al., 2023). Therefore, to mitigate such risks, the BHP was constrained at 90% of the mud weight, ensuring a 10% safety factor (**Figure 10**):
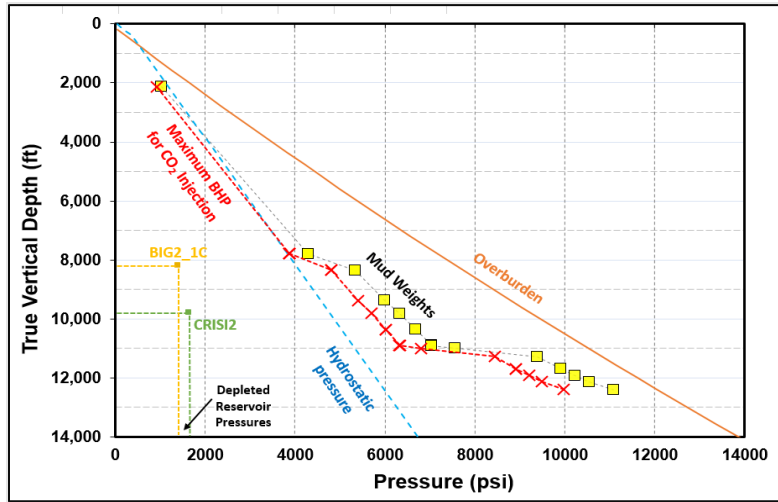
Figure 10 Overburden and hydrostatic pressure variations with depth in VR014. The mud weight and the corresponding maximum BHP set for CO₂ injection can be found in the figure. Lastly, the depleted pressures of two reservoirs are indicated based on pressure survey data (BOEM)

Trapping Mechanisms

This work primarily focuses on structural, residual, and solubility trapping mechanisms. Structural trapping refers to storing CO_2 within geological formations either as a supercritical fluid or as a free gas. If the integrity of the caprock or sealing faults is compromised, the structurally trapped CO_2 would tend to flow and escape from these geological structures (Punnam et al., 2021). On the other hand, residual trapping involves immobile gas stuck in the pores and pore throats due to capillary forces. This process is crucial for secure CO_2 storage as it keeps the immobilized gas separated from the caprock, enhancing the safety of the storage process (Krevor et al., 2015). Finally, solubility trapping is another primary driving force behind CO_2 storage, especially in saline aquifers where a substantial amount of gas might solubilize in brine. When CO_2 dissolves in brine, it undergoes decomposition into H^+ and HCO_3^- ions, which subsequently engage in reactions with existing minerals (Meng et al., 2014). These reactions, contingent upon the mineral composition of the formation, may prompt the formation of carbonate minerals like calcite, dolomite, and siderite (Nghiem et al., 2009).

In our study, the conventional Land's model was utilized to accommodate relative permeability hysteresis and evaluate residual trapping (Land, 1968). The Land trapping coefficient (C) is formulated as follows (8):

$$C = \frac{1}{S_{gt,max}} - \frac{1}{S_{g,max}} \tag{8}$$

where $S_{g,max}$ represents the maximum possible gas saturation in the system and $S_{gt,max}$ is the maximum trapped gas saturation. Our work utilized the maximum gas saturation ($S_{g,max}$) of 0.68. On the other hand, an average C of 1.39 and the corresponding $S_{gt,max}$ of 0.35 were considered in our study based on the literature-reported values (Krevor et al., 2015).

Furthermore, solubility trapping was modeled as a phase equilibrium process dictated by the balance of fugacities between the gas and aqueous phases (10):

$$f_{i,g} - f_{i,aq} = 0 \tag{10}$$

where $f_{i,g}$ and $f_{i,aq}$ are the fugacities of component i in the gas and aqueous phases, respectively. While $f_{i,g}$ is determined using an equation of state (EOS) (Peng and Robinson 1976), the calculation of $f_{i,aq}$ is based on Henry's law (Li and Nghiem 1986):

$$f_{i,aq} = y_{i,aq}H_i \qquad (11)$$

where $y_{i,aq}$ is the mole fraction of component i in the aqueous phase and H_i is Henry's law constant, which depends on temperatures, pressures, and salinities in the system (Zhang et al., 2023). Liquid and gas properties were characterized with the CMG-WinProp™ phase behavior simulator at the embedded pressures and the average temperature of 200 °F.

Results & Discussion

This section thoroughly examines petrophysical models and seismic attributes to accurately appraise the quality of the targeted reservoirs, gaining detailed insights into their characteristics. The focus will then shift to dynamic simulations of CO_2 injection and storage in the VR014 field, revealing crucial findings into CO_2 trapping mechanisms. These findings highlight the field's potential for secure CO_2 storage, providing essential considerations for effective reservoir development strategies.

Geostatistical Model and Seismic Attributes

The VR014 reservoirs are categorized as good to very good reservoir quality. The reservoir zones generally exhibit medium to high porosity, low to medium shale volume values, and net-to-gross ratios. Calculated porosities correlate well with core analysis results, although they are slightly lower, possibly attributed to core unloading and core plug drying effects.

The inverted AI reveals the sand's continuation and their respective quality where the sand within the study area is changing as it was deposited in a complex deltaic slope with dominating channels (**Figure 11 Top**). Inversion derived porosity confirms that the field is within the highest-quality sand sequence. The main major faults. The impedance slices at seal levels integrated with *Vsh* show possible weaknesses in the seal (**Figure 11 Bottom**). However, they do not directly overlay the structural high (highest pressures), thus the risk is not considered significant to the trapping mechanism.
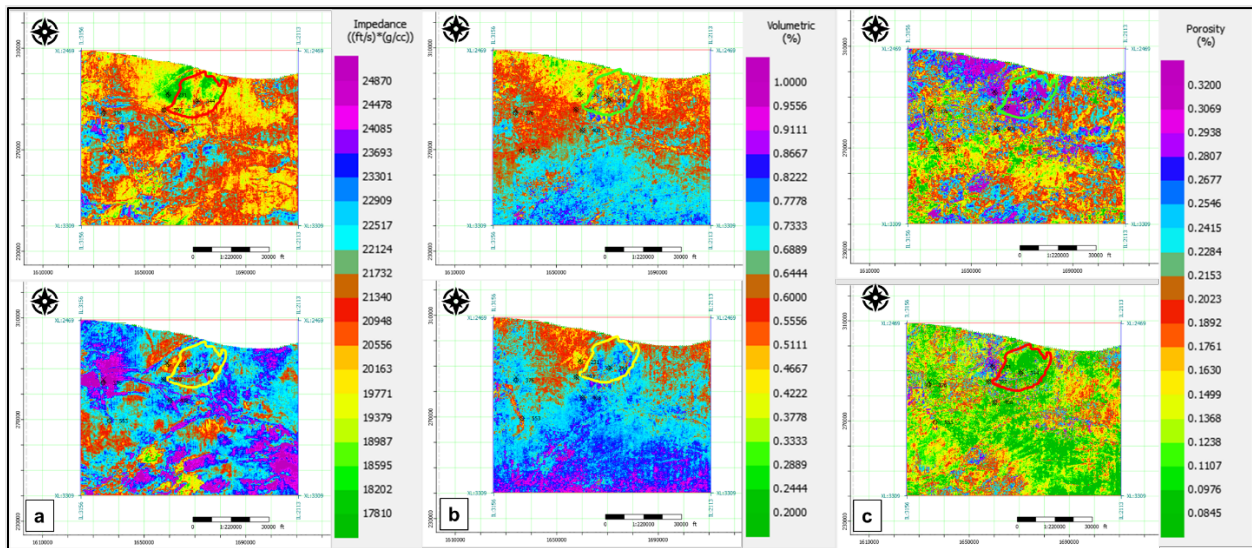

Figure 11 Exported inversion property time slices. a) acoustic impedance, b) Vsh, c) Phie, at both reservoir (top row) and seal window (bottom row) for BIG2_1C system. Field geometry highlighted in different colors overlay to illustrate the property distribution on field scale.

Selected extracted seismic attributes at seal and reservoir level are presented on (**Figure 12**). Although affected by acquisition footprint BIG2_1C seal presents a generally low amplitude background particularly around the VR14 field area, in agreement with the consistent shaly facies found at the well. The exception of a noticeable channel pattern on the bottom left corner, also visible on the corresponding spectral

decomposition display (**Figure 13b**) corresponding to a known thief zone around field VR39. By contrast, extracted attributes at BIG2_1C reservoir level (**Figure 12b**) present high amplitudes displays centered around VR14 structural high and likely represent the hydrocarbon effect at time of seismic acquisition.
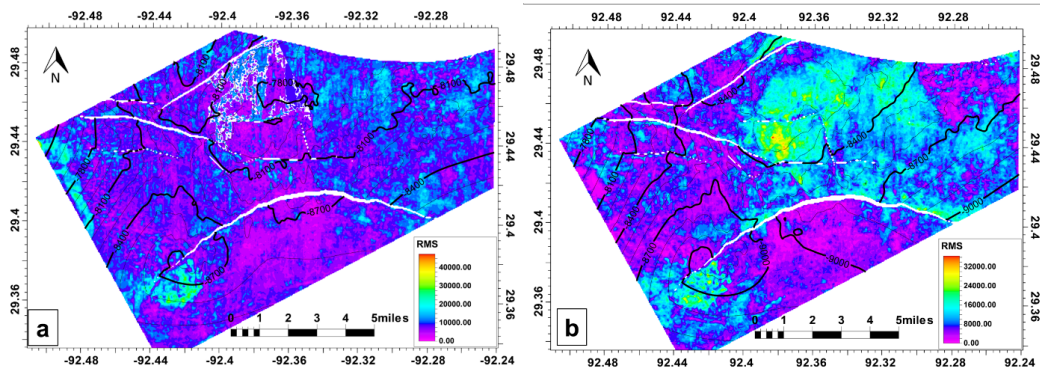

Figure 12: Seismic attributes extracted at BIG2_1C a) RMS seal level and at BIG2_1C Reservoir level b) RMS, c) envelope, and d) energy attenuation.
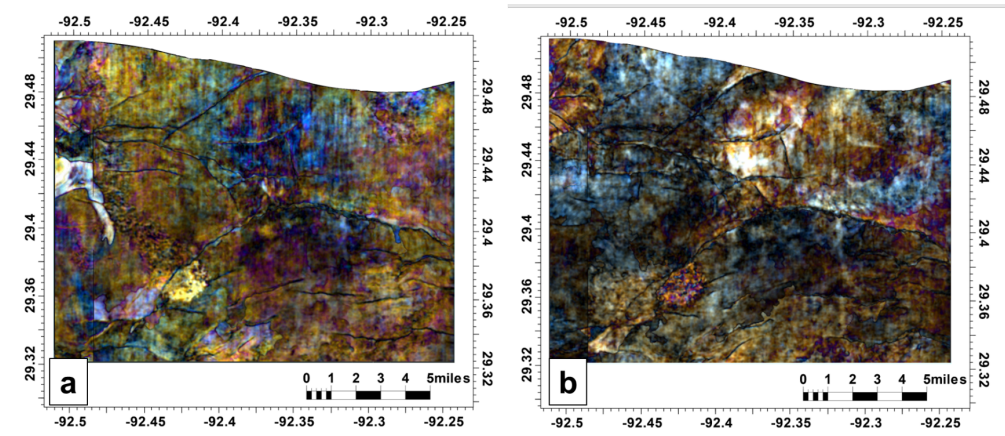

Figure 13: Spectral decomposition of BIG2_1C at a) seal level (15-25-35Hz) and b) reservoir level (25-30-35Hz)

Petrophysical models were developed to represent various interpreted petrophysical parameters. Cross-sections were extracted from these models in a west-northwest to east-southeast (NW-SE) direction to delineate reservoir quality. The constructed petrophysical models and cross-sections, in addition to inverted porosities from seismic (**Figure 11**), provide a clear indication of the reservoir quality within the studied area.

The facies model shows that the BIG2_1C reservoir consists of 70% sand, 24% silt, and 6% shale, while CRISI2 is siltier as analysis shows 64% sands and 36% silts. These silts are relatively porous but characterized by lower permeability, which can impact injectivity. The effective porosity model for the VR014 field indicates values ranging from 0.12 to 33.1% at the BIG2_1C reservoir and 0.07 to 33.7% at the CRISI2 reservoir. Around 65% of the model demonstrates effective porosity exceeding 20%, with lower values mainly observed in the southern portion of the study area as lower sands are deposited. The shale volume model generally depicts intermediate to high values ranging from 10 to 98%, with approximately 62% of the model showing shale volume between 24 and 56%. The depleted water saturation values in the model range from 55 to 100%, with 85% of the model exhibiting high water saturation (70–94%) at reservoir intervals. The permeability in both reservoirs exhibit similar ranges as they deposited in similar environmental conditions, ranging between 20- 3452 mD and 59% with permeabilities over 1000 mD at reservoir intervals. The net-to-gross model spans values from 60 to 100%, with approximately 68% of the model falling around 74% N/G ratio. The unproduced gas reserves are low, characterized by high water

saturation, and highly concentrated in the structural height of the field, which is validated by high water production and pressure depletion of the reservoir. BIG2_1C reservoir has a uniform geometry and thickness. However, the CRISI2 reservoir is asymmetrical where the highest thickness is in the western areas and pinches out towards the southern parts.

The fault planes show varying SGR (Shale Gouge Ratio) values within the range of 0.09 to 0.97. Approximately 39% of these fault planes have SGR values falling between 0.4 and 0.6. The fault permeability of the field ranges from 0.001 to 10 mD, with about 95% of the fault planes exhibiting values between 0 and 0.55 mD. These SGR and fault permeability values collectively suggest that the fault planes possess intermediate to low permeability for minor faults, indicating semi to impermeable characteristics. Meanwhile, the major listric fault is characterized by higher SGR and lower permeabilities and therefore expected to be fully sealing. Two primary clusters in fault transmissibility multipliers become apparent. The first cluster, encompassing 55% of the fault planes, has transmissibility values ranging from 0 to 0.23. In contrast, the second cluster, representing 45% of the fault planes, exhibits transmissibility values between 0.5 and 0.85, corresponding to the major faults with high displacement and minor faults group with lower throw. Consequently, most fault planes were deemed impermeable, with only a small percentage exhibiting permeable characteristics.

Dynamic Reservoir Simulation – CO$_2$ Plume Migration

A thorough understanding of the CO$_2$ plume's behavior is essential for effective reservoir management and ensuring the viability of long-term storage. The geological complexity, marked by layered reservoirs, caprocks, and surrounding faults, underscores the significance of our investigation. In this subsection, we initiate our dynamic simulation discussion with a detailed examination of the migration of the injected CO$_2$ plume within the model, focusing particularly on the BIG2_1C and CRISI2 reservoirs in the VR014 field. This sets the stage for a meticulous analysis of the CO$_2$ front and its propagation dynamics during injection and subsequent storage phases, providing valuable insights into key aspects of reservoir response and the efficacy of CO$_2$ containment strategies.

Figure 14 and **Figure 15** depict the distribution and evolution of gas saturation within the BIG2_1C and CRISI2 reservoirs, respectively. These illustrations capture three distinct stages: the initial state before the commencement of injection in 2025, the completion of the injection phase in 2075, and the conclusion of the storage phase in 2175.
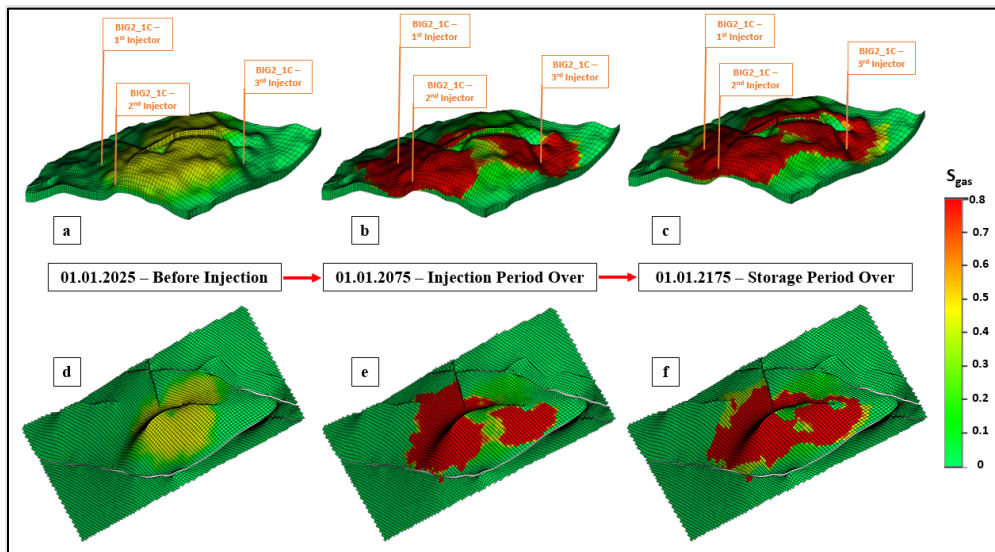

Figure 14 Gas front propagation at three stages in the BIG2_1C reservoir: a, b, and c represent the cropped 3D view of the reservoir, while d, e, and f offer the corresponding aerial perspectives.
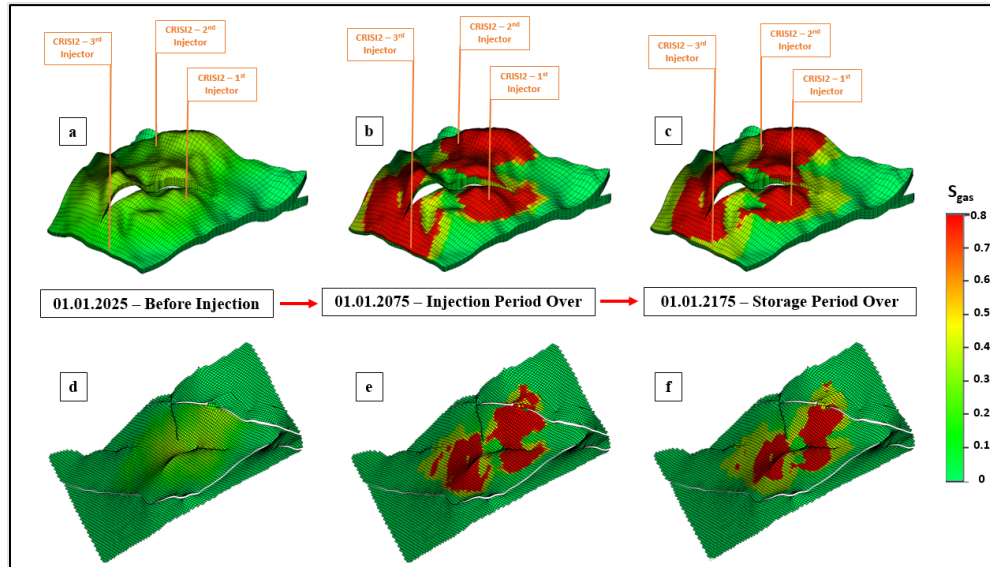
Figure 15 Gas front propagation at three stages in the CRISI2 reservoir: a, b, and c represent the cropped 3D view of the reservoir, while d, e, and f offer the corresponding aerial perspectives.

Our dynamic simulations underscore the pivotal role of strategic well placement in ensuring successful gas storage and injectivity, with gas efficiently propagating in porous media characterized by favorable petrophysical properties. Moreover, our findings confirm the increased efficiency of injecting into thicker sections of a reservoir and closer to the water leg, evident in higher final gas saturation and total gas trapping. This efficacy arises from the observed trend where, upon concluding injection, a substantial portion of the gas escapes to the highest points in the reservoir during the storage phase, as shown in **Figure 14b** and **Figure 14c**. Notably, significant gas volumes injected into the lower regions of depleted reservoirs migrated to the higher section of the anticline system in 2075–2175, potentially enhancing solubility trapping. Additionally, a comparison between **Figure 15e** and **Figure 15f** reveals a gradual reduction in gaseous CO_2 saturation during the storage phase, particularly in the CRISI2 reservoir, signifying its dissolution in the brine and residual entrapment following the cessation of the injection phase in 2075.

Dynamic Reservoir Simulation – CO₂ Injectivity and Seal Performance

Injectivity pertains to the ease with which fluid can be introduced into a storage medium without causing formation fractures (Raza et al., 2015). Stratigraphic factors, including permeability and thickness, play a crucial role in influencing the quality of the injection process. However, while high permeability can accelerate CO_2 migration, it may simultaneously reduce the effective storage capacity of the medium.

Proper management of injectivity is essential to prevent the initiation of fractures in the storage medium. Hence, we aimed to maintain injection pressures well below the assumed formation fracture pressure, aligning them with the mud weights employed at corresponding depths to ensure secure gas storage. **Figure 16** illustrates the 3D pressure distribution in our simulation model before and after CO_2 injection.
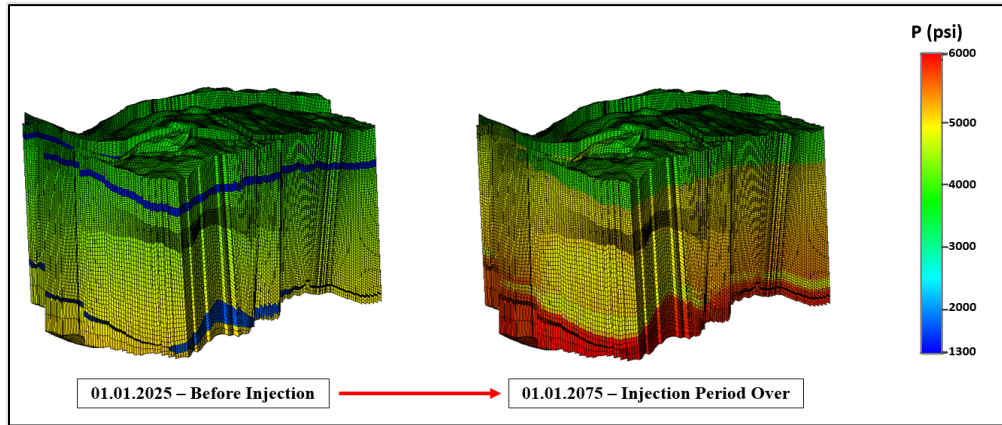
Figure 16 Pressure distribution in the 3D simulation model before and after the injection phase.

As seen in **Figure 16**, initiating CO_2 injection into the depleted reservoirs results in a gradual rise in reservoir pressure, impacting the pressures of the surrounding formations as well. This anticipated pressure elevation, stemming from the introduction of CO_2 into the porous media, necessitates further examination of pressures in the simulation model. Their comparison with fracture pressures at the corresponding depths is essential for managing injectivity effectively and preventing fracturing. **Figure 17** provides visuals of the bottom hole pressures (BHP) in the BIG2_1C and CRISI2 reservoirs, along with the corresponding assumed fracture pressures. This indicates that there is a considerable pressure window between BHP and fracture pressure in each reservoir, ensuring safe CO_2 injection.
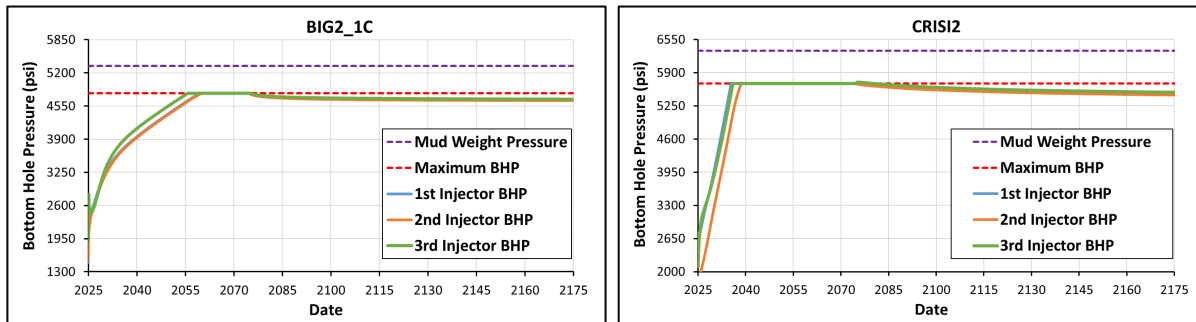

Figure 17 Bottom hole pressures for: BIG2_1C (left) and CRISI2 (right) injectors.

Observably, when the injection pressures approach the maximum allowable limit (set at 90% of mud weight pressure), the injection rate is subsequently reduced. This adjustment serves to counterbalance the pressure increase, enabling the continuation of injection without surpassing the established threshold. This precautionary measure mitigates the risk of fracturing the surrounding formations.

Another crucial aspect investigated in this study is the sealing capacity of caprocks and faults. The findings indicate that the caprock associated with BIG2_1C exhibits excellent sealing capacity, with minimal gas flow observed even in the deepest layer of its upper seal. Conversely, the sealing performance of the upper seal in the CRISI2 reservoir is compromised. Specifically, it was observed that some gas does penetrate the deepest layer of its caprock (K = 68/76), attributed to an excess of silt minerals in that region. However, upon closer examination, it was noted that the vertical movement of gas is significantly impeded in the penultimate layer of the CRISI caprock (K = 67/76). Consequently, although the caprock of CRISI demonstrates inferior performance compared to BIG2_1C, there is no significant risk of CO_2 escaping through the overburden to shallower depths.
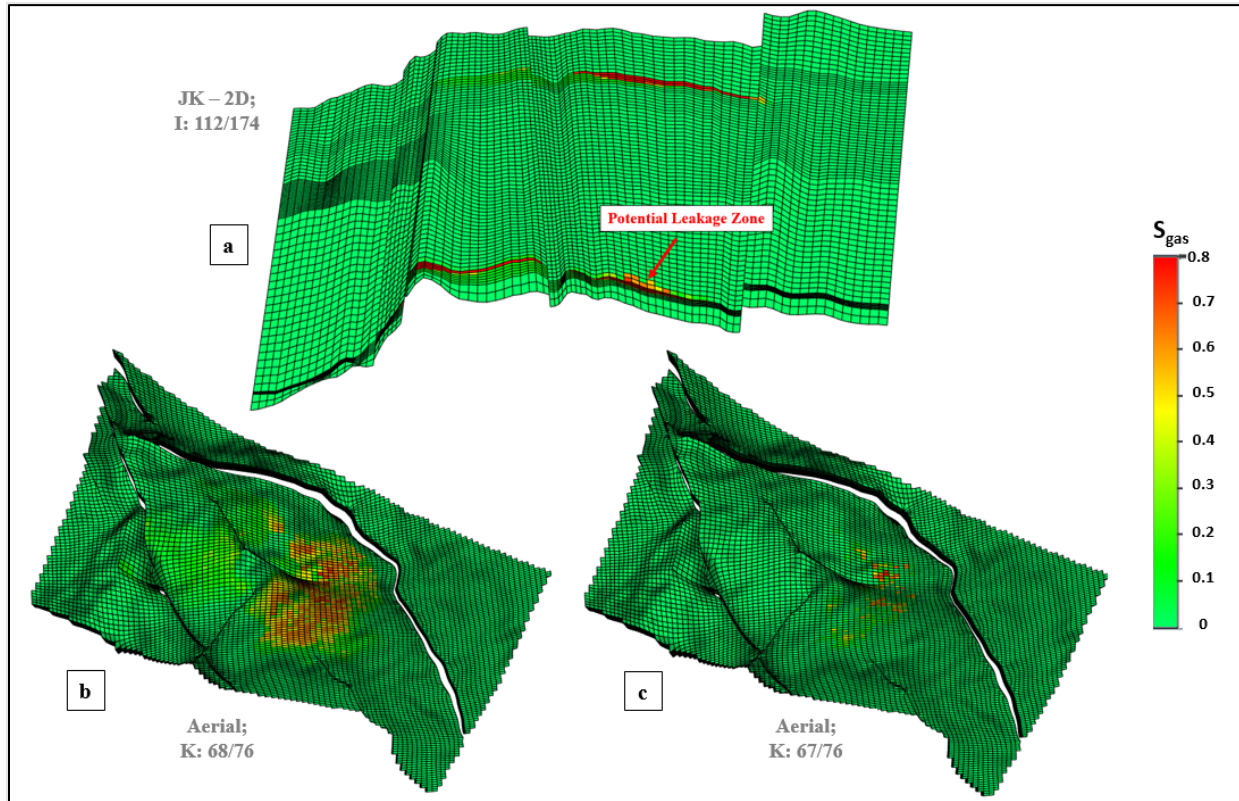
Figure 18 Evaluation of the sealing capacity of caprocks based on gas saturation in the end of the storage phase: a) vertical cross-section illustrating vertical gas propagation; aerial view of the: b) ultimate layer (K=68/76) and c) penultimate layer (K=67/76) of the CRISI2 upper seal showing a decreasing amount of gas penetrating up through the caprock.

Dynamic Reservoir Simulation – Amount of Injected and Trapped CO$_2$

The dynamic simulation explored active CO$_2$ trapping mechanisms, which include structural trapping under the caprock, dissolution in gas and brine, and residual trapping, as shown in **Figure 14 and Figure 15**. The observed decline in the supercritical mobile CO$_2$ phase (structural trapping) and an increase in dissolved and residually trapped CO$_2$ in **Figure 19** are expected to continue over time since greater parts of the reservoir are contacted by the mobile CO$_2$ plume trying to reach equilibrium. Due to capillary forces, part of that mobile CO$_2$ stays trapped permanently within the pores. While in contact with the remaining reservoir fluids, the supercritical and residually trapped CO$_2$ are affected by dissolution effects in the form of solubility trapping. Here, CO$_2$ gets dissolved in the brine and is no longer in supercritical condition, resulting in a reduction of the supercritical CO$_2$ as time passes. Additionally, while being dissolved, the CO$_2$ available to be residually trapped is less, resulting in a reduction of the residual trapping potential of CO$_2$. The greatest rate of dissolution happened during the first 75 years, explaining the stabilization in the solubility trapping curve. It's important to mention that solubility trapping, driven by the molecular diffusion at the interface of the formation fluids and free gas, is a slow process that takes longer to happen due to the small molecular diffusion coefficient. Its contribution to the trapping potential gets maximized after more than a few hundreds of years, and it is believed that it may take thousands of years for the gas to fully dissolve in brine, which is why we might not see the impact on the investigated scale of this study.
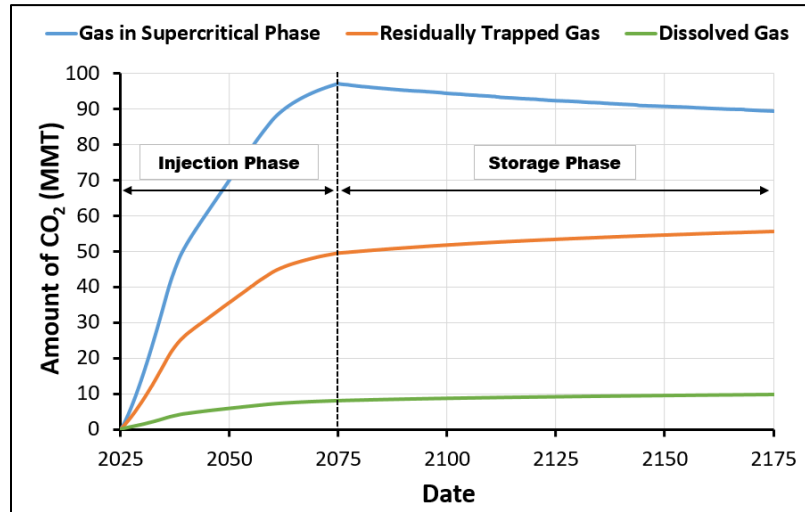
Figure 19 Evaluation of trapped and supercritical/free gas quantities over time.

As observed in **Figure 19,** by 2075, 154.73 million of metric tons of CO_2 had been injected into the reservoir, from which 62.83% (97.216 MMT) was trapped structurally as a supercritical gas mobile phase, 5.17% (8.014 M) was dissolved and 32% (49.5 MMT) was residually trapped as an immobile gas phase. By 2175, 100 years of residence time post-injection, 6.29% (9.732 MMT) had been dissolved, 35.89% (55.539 MMT) trapped residually, and 57.82% (89.459 MMT) in the gaseous mobile phase. All these values are summarized in **Table 4.**

Table 4 Summary of the injected and trapped CO_2 at the end of the injection phase (2075) and storage phase (2175).

Amount of CO_2, megatons (MMT)	2075	2175
Mobile/Supercritical Gas	97.216	89.459
Residually Trapped Gas	49.5	55.539
Dissolved Gas	8.014	9.732
Total Injected Gas	154.73	154.73

Conclusions

The VR014 field, encompassing the BIG2_1C and CRISI2 reservoirs, is suitable for sustainable carbon capture and storage (CCS). These findings shed light on the distribution and fate of injected CO2 within the VR014 field and their implications for long-term CO2 storage. The BIG2_1C reservoir system is characterized by a good, continuous, thick, high-quality shaly seal. Meanwhile, the CRISI2 reservoir system has a relatively thicker but more silty-dominated shale interval. This can serve as a potential leak path to shallower parts of the system. The faults were not recognized as potential risks as the analysis found them impermeable, and the trapping mechanism is not mainly fault-dependent. Thus, no high pressures are expected or recognized in the dynamic model close to the faults. Therefore, the VR014 field was deemed suitable for sustainable CCS at two depleted reservoir levels that can maintain a significant amount of CO2 safely stored for the upcoming millions of years. Evaluating the transmissibility of faults is essential to mitigate leakage risks. In the VR014 field, low transmissibility was encountered at major fault planes. This plays a major role in reducing the risk of leakage, demonstrating the importance of detailed geological assessment. Dynamic simulation is crucial for predicting CO2 behavior post-injection. It helps in understanding how CO_2 will disperse, interact with reservoir fluids, and the extent of its movement within the reservoir. Various trapping mechanisms, such as structural, solubility, and residual trapping, play a vital role in ensuring the long-term sequestration of CO_2. The effectiveness of these mechanisms is influenced by reservoir properties and fluid dynamics.

The study highlights that depleted reservoirs can be repurposed for large-scale CCS, providing a sustainable approach to reducing atmospheric CO_2 levels, securely storing substantial amounts of CO_2.

Acknowledgments

References

Agartan, E., Gaddipati, M., Yip, Y. et al. 2018. CO2 storage in depleted oil and gas fields in the Gulf of Mexico. *International Journal of Greenhouse Gas Control* **72**: 38-48.

Alonso, C., Boudreau, L., Cross, K. et al. Identification of Tier 1 Depleted Reservoirs in the Gulf of Mexico. *Bureau of Ocean Energy Management*, https://www.boem.gov/sites/default/files/documents/about-boem/BOEM-Depleted-Reservoir.pdf.

Fathy, A., Adila, A., Ahmed, S. et al. 2023. Effects of Rock Heterogeneity and Wettability on CO2 Mineralization During Storage in UAE Depleted Carbonate Gas Formations. *Proc.,* Abu Dhabi International Petroleum Exhibition and ConferenceD031S116R005.

Fathy, A., Arif, M., Adila, A. S. et al. 2023. Quantitative Assessment of CO2 Mineral Trapping Capacity in Presence of Sealing Fault in Carbonate Sequences: A Numerical Approach. *Proc.,* Gas & Oil Technology Showcase and Conference.

Hannis, S., Lu, J., Chadwick, A. et al. 2017. CO2 Storage in Depleted or Depleting Oil and Gas Fields: What can We Learn from Existing Projects? *Energy Procedia* **114**: 5680-5690.

Krevor, S., Blunt, M. J., Benson, S. M. et al. 2015. Capillary trapping for geologic carbon dioxide storage–From pore scale physics to field scale implications. *International Journal of Greenhouse Gas Control* **40**: 221-237.

Land CS. Calculation of Imbibition Relative Permeability for Two- and Three-Phase Flow From Rock Properties. *SPE Journal* 1968;**8**:149–56.

Larionov, V. 1969. Borehole radiometry. *Nedra, Moscow* **127**: 813.

Li, Y. K. and Nghiem, L. X. 1986. Phase equilibria of oil, gas and water/brine mixtures from a cubic equation of state and Henry's law. *The Canadian Journal of Chemical Engineering* **64** (3)

Manzocchi, T., Walsh, J., Nell, P., and Yielding, G. 1999. Fault transmissibility multipliers for flow simulation models. *Petroleum Geoscience* **5** (1): 53-63.

Meng, Q. and Jiang, X. 2014. Numerical analyses of the solubility trapping of CO2 storage in geological formations. Applied energy 130: 581-591.

Nghiem, L., Shrivastava, V., Tran, D. et al. 2009. Simulation of CO2 storage in saline aquifers. *Proc.,* SPE/EAGE reservoir characterization and simulation conference.

Peng, D.-Y. and Robinson, D. B. 1976. A new two-constant equation of state. *Industrial & Engineering Chemistry Fundamentals* **15** (1): 59-64.

Pickett, G. R. 1972. *Practical formation evaluation*: GR Pickett.

Punnam, P. R., Krishnamurthy, B., and Surasani, V. K. 2021. Investigations of structural and residual trapping phenomena during CO2 sequestration in Deccan volcanic Province of the Saurashtra region, Gujarat. International Journal of Chemical Engineering 2021: 1-16.

Raza, A., Rezaee, R., Gholami, R. et al. 2015. Injectivity and quantification of capillary trapping for CO2 storage: A review of influencing parameters. Journal of Natural Gas Science and Engineering 26: 510-517.

Russell, B. H. 1988. *Introduction to seismic inversion methods*: SEG Books.

Ushie, F. 2001. Formation water resistivity (Rw) determination: the SP method. *Journal of Applied Sciences and Environmental Management* **5** (1).

Veeken, P. and Da Silva. 2004. Seismic inversion methods and some of their constraints. *First break* **22**

Wendt, A., Sheriff, A., Shih, C. Y. et al. 2022. A multi-criteria CCUS screening evaluation of the Gulf of Mexico, USA. *International Journal of Greenhouse Gas Control* **118**: 103688.

Yielding, G., Freeman, B., and Needham, D. T. 1997. Quantitative fault seal prediction. *AAPG bulletin* **81** (6): 897-917.

Zhang, H., Al Kobaisi, M., and Arif, M. 2023. Impact of wettability and injection rate on CO2 plume migration and trapping capacity: A numerical investigation. *Fuel* **331**: 125721.